

Received May 29, 2014, accepted June 26, 2014, date of publication August 28, 2014, date of current version September 10, 2014.

Digital Object Identifier 10.1109/ACCESS.2014.2351751

Rectangular Fixed-Gantry CT Prototype: Combining CNT X-Ray Sources and Accelerated Compressed Sensing-Based Reconstruction

BRIAN GONZALES¹, DERREK SPRONK¹, YUAN CHENG¹, ANDREW W. TUCKER¹, MORITZ BECKMAN¹, OTTO ZHOU², AND JIANPING LU²

¹XinRay Systems Inc, Research Triangle Park, NC 27709 USA

²Xintek Inc., Research Triangle Park, NC 27709 USA

Corresponding author: B. Gonzales (bgonzales@xinraysystems.com).

This work was supported by the U.S. Department of Homeland Security, Science and Technology Directorate, under Contract HSHQDC-09-C-0016.

ABSTRACT Carbon nanotube (CNT)-based multibeam X-ray tubes provide an array of individually controllable X-ray focal spots. The CNT tube allows for flexible placement and distribution of X-ray focal spots in a system. Using a CNT tube, a computed tomography (CT) system with a noncircular geometry and a nonrotating gantry can be created. The noncircular CT geometry can be optimized around a specific imaging problem, utilizing the flexibility of CNT multibeam X-ray tubes to achieve the optimal focal spot distribution for the design constraints of the problem. Iterative reconstruction algorithms provide flexible CT reconstruction to accommodate the noncircular geometry. Compressed sensing-based iterative reconstruction algorithms apply a sparsity constraint to the reconstructed images that can partially account for missing angular coverage due to the noncircular geometry. In this paper, we present a laboratory prototype CT system that uses CNT multibeam X-ray tubes; a rectangular, nonrotating imaging geometry; and an accelerated compressed sensing-based iterative reconstruction algorithm. We apply a total variation minimization as our sparsity constraint. We present the advanced CNT multibeam tubes and show the stability and flexibility of these new tubes. We also present the unique imaging geometry and discuss the design constraints that influenced the specific system design. The reconstruction method is presented along with an overview of the acceleration of the algorithm to near real-time reconstruction. We demonstrate that the prototype reconstructed images have image quality comparable with a conventional CT system. The prototype is optimized for airport checkpoint baggage screening, but the concepts developed may apply to other application-specific CT imaging systems.

INDEX TERMS Carbon nanotube x-ray sources, iterative reconstruction, compressed sensing reconstruction, total variation minimization, fixed-gantry computed tomography.

I. INTRODUCTION

Conventional X-ray tubes are thermionic or “hot” sources, meaning that the cathode, a metal filament in this case, is heated up to produce electrons which are subsequently accelerated toward the anode to produce X-rays. An alternative to thermionic sources is field emission sources or “cold” sources. In field emission tubes, electrons are extracted from the tip of the object through a process called quantum tunneling [1]. These electrons are then accelerated toward the anode for X-ray production. Field emission electron sources provide three main advantages over conventional thermionic electron sources: (1) they operate at room temperature,

(2) they can be electronically controlled, and (3) they have an instantaneous response. The main concerns with field emission sources are tube lifetime and maximum power. More recently, carbon nanotubes (CNTs) have been developed for use as field emitters in these X-ray sources [2], [3]. Due to their large aspect ratios and thermal and conductive stability, CNTs make ideal field emitters. CNT X-ray sources have been shown to have long lifetimes [4], X-ray tube currents as high as 1 ampere [5], and have been operated at anode potentials as high as 160 kVp [6].

Recent applications of CNT based multibeam X-ray tubes to tomographic imaging systems have demonstrated

significant improvement in image quality [4], [7] and increased flexibility in system design [8]–[10]. CNT multibeam tubes generate a spatially distributed array of individually controllable X-ray focal spots within a single vacuum tube [11]. By sequentially scanning each focal spot, a tomographic scan of an imaged object is acquired with no movement of the source [12]. Generating a tomographic scan without moving the X-ray source removes motion-induced blurring, resulting in increased resolution in the reconstructed images. The spatial distribution of X-ray focal spots within the multibeam tube determines the geometry of the tomographic scan, as compared to the physical rotation of an X-ray source. By removing the need to physically move an X-ray source, new imaging geometries such as rectangular tomosynthesis [9] or rectangular computed tomography (CT) [10] can be explored.

The first tomographic application of CNT X-ray sources was a micro computed tomography (micro-CT) system for imaging small animals [13]. The micro-CT uses only a single X-ray focal spot and a flat panel detector array. The X-ray focal spot and detector rotate around the subject to acquire the CT data. The CNT X-ray source technology uses field emission rather than thermal emission to generate the free electrons required to produce X-rays [2]. The use of field emission allows the X-ray source to be rapidly and precisely pulsed. The CNT X-ray source is pulsed to align the X-ray projections with the imaged subject's cardiac or respiratory cycles, providing higher resolution images [14]. The use of field emission also allows for close spacing between electron emitters because the process does not produce excess heat. The close spacing of electron emitters allows a dense array of X-ray focal spots to be generated in a single tube. The micro-CT system only takes advantage of the fast pulsing properties of the CNT X-ray sources.

The use of CNT multibeam X-ray sources for a fixed (non-rotating) gantry CT was explored by Quan and Lalush [16], [17] for a micro-CT application. In [16], Quan and Lalush investigated two new CT imaging geometries: a square geometry using two linear arrays of X-ray focal spots and two linear detector arrays, and a hexagonal geometry incorporating three shorter linear arrays of X-ray focal spots and three shorter linear detector arrays. Both imaging geometries have uneven angular coverage because the X-ray focal spots are not circularly arranged, resulting in a portion of the image region not being covered by a full 180° span. Quan and Lalush show that high quality images can be reconstructed using iterative reconstruction algorithms but significant artifacts remained due to the missing angles. In [17], Quan and Lalush present a modified ordered-subset convex (MOSC) algorithm derived from the ordered subset convex reconstruction method [18], [19] and modified to increase the reconstruction speed. In these initial studies, the geometries were simulated based on the properties of the CNT multibeam X-ray sources.

The simulation studies' reconstructions showed image artifacts due to missing data. These artifacts are similar to other

sparse-view or limited-angle CT images [20]. Sparse-view CT is used as a dose reduction method in medical CT; by reducing the number of X-ray projection views, the total subject dose is reduced. The concept of sparse-view CT along with the iterative reconstruction methods required to create a reconstructed image using sparse data has existed for years [21]. The challenge for sparse-view CT is that the reduction in dose results in increased noise in the reconstruction and the missing angles create artifacts [22]. A compressed sensing approach has been proposed to suppress the artifacts and noise while maintaining resolution in the reconstructed images [23].

A compressed sensing approach attempts to recover an undersampled signal by assuming that the signal is sparse in some domain. Iterative reconstruction algorithms define the three-dimensional image volume as a set of unknowns, commonly represented as image voxels. The image voxels represent a regular sampling over a large region which for sparse-view CT is an undetermined problem with no absolute solution. A compressive sensing approach reduces the solution space by imposing a measure of sparsity in the reconstructed images. A typically used measure of sparsity is an l -norm of the image or image gradient [24]. An l_0 norm represents the truest sparsity by separating the number of non-zero elements from the zero elements in the image and restricting the number of non-zero elements in the final reconstruction, thereby reducing the total noise in the image [25]. The l_1 norm represents the total sum of the image and when combined with the gradient image, is a measure of the total variation (TV) in the image [26]. The TV in the reconstructed images should be limited to the object boundaries, and minimizing the TV in the reconstructions reduces inherent noise and artifacts. Compressed sensing-based reconstruction methods continue to be an active field of research for a wide range of CT geometries [27]–[29].

A key limitation to compressed sensing iterative reconstruction methods is the time it takes to reconstruct a volume. These methods require multiple projections and back projections although with complex image domain operations to impose the sparsity constraints. Graphics Processing Units (GPUs) have been proposed as a method to accelerate iterative reconstruction methods [30] and compressed sensing-based reconstruction methods [31]. The GPU architecture is designed with hundreds to thousands of parallel cores that can be programmed to apply the same mathematical process to different pieces of data simultaneously. By exploiting the parallel architecture, computationally expensive steps such as image projection and back projection can be performed simultaneously, significantly reducing the overall reconstruction time [32].

The first CT imaging setup developed by XinRay Systems Inc used two CNT multibeam X-ray tubes to form a rectangular geometry and used a compressive sensing iterative reconstruction algorithm implemented on a GPU [10]. This imaging setup was designed to characterize the imaging challenges to a sparse-view fixed gantry rectangular CT geometry.

The uneven distribution of X-ray dose was addressed by rebinning the projection data into a parallelized sinogram. The missing angle artifacts were addressed using a total variation constraint applied with an algebraic iterative reconstruction technique (ART). The scatter was addressed by including a simple model of the scatter in the forward projection model. Scatter was identified as a key challenge because the fixed gantry geometry precluded the use of an anti-scatter grid.

In this paper, we present a laboratory prototype CT that is based on the previously described imaging setup. The prototype uses CNT multibeam tubes arranged in a fixed gantry rectangular imaging geometry. The imaging geometry uses a sparse-view implementation to achieve higher imaging speeds. The laboratory prototype has an improved imaging geometry and a further improved and accelerated reconstruction method. The laboratory prototype achieves better image quality compared to the first imaging setup. In this paper, we will present the new CNT multibeam X-ray tubes used by the laboratory prototype scanner, the geometry improvements implemented to optimize the number and distribution of X-ray focal spots, and the new reconstruction method developed to improve the reconstructed image quality while increasing the reconstruction speed. We will also present initial imaging results and compare the image results to a similar scan taken on a conventional CT.

II. CNT MULTIBEAM X-RAY TUBES

We have developed a new CNT multibeam X-ray tube optimized for airport baggage screening CT. Screening CT systems require large tunnels (up to 1 meter width) and need high-power X-ray tubes so that satisfactory signal to noise levels are attained at the detector when the X-rays travel along the path length and are considerably attenuated by the objects being screened. Continuous operation at 1000 watts has been challenging since power of this level necessitates the use of an anode cooler, which is typically bulky and difficult to integrate into a high speed rotating gantry.

In this paper, we demonstrate that multibeam field emission X-ray (MBFEX) tubes can output continuous X-ray power greater than 3 kilowatts with a small focal spot size and excellent stability at 160kV (Fig. 1). The focal spot size as full

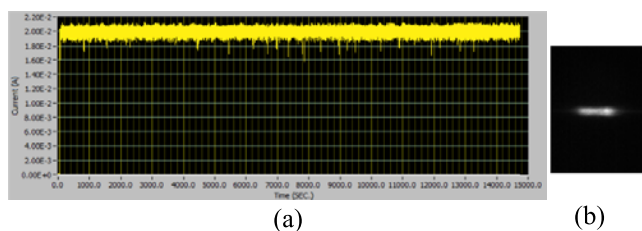


FIGURE 1. Experimental results showing the current and focal spot for our new MBFEX tube. (a) Stable mean anode current (~ 20 mA) with respect to time at 160kV as measured by the anode power supply. (b) Pin-hole image of one of the focal spots of the high power tube (taken with 0.1 mm pin-hole).

width at half maximum (FWHM) of the tube has a mean value of 2.6 mm in the x direction and 0.5 mm in the z direction with a standard deviation of 0.4 mm in the x direction and 0.1 mm in the z direction. The z direction is the conveyor belt travel direction.

The MBFEX tube tested was developed for both airport checked baggage screening and airport carryon baggage screening applications. These MBFEX tubes have the potential to enable a new generation of high throughput and small footprint inline explosives detection systems (EDS) for baggage screening. The tube was designed to have continuous operating power up to 4000 W and is supported by an anode oil cooling system. This operating power should generate sufficient photon flux for CT imaging with thin slices at the high belt speed necessary for handling up to 1000 bags per hour. Each MBFEX tube has 250 individual focal spots that can cover one side of a one meter wide tunnel, although all focal spots may not be operated depending on the imaging application. A picture of the prototype MBFEX tube is shown in Fig. 2.

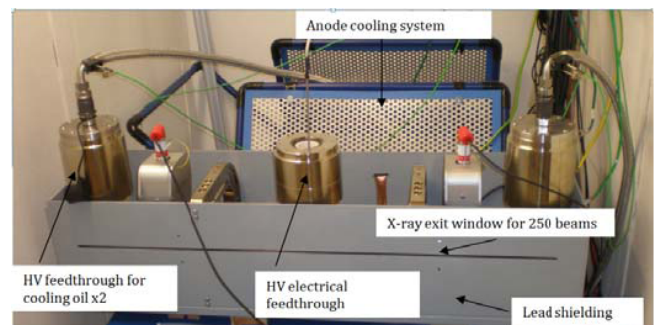


FIGURE 2. Picture of the MBFEX prototype tube and anode cooling system (top cover of the lead shielding not shown).

The prototype MBFEX tube tested was integrated into a prototype stationary checkpoint CT scanner (Section III) with a tunnel size smaller than 1 meter. The smaller tunnel size does not require the full meter of coverage and a portion of the 250 beams are not in the field of view of the detector array. Out of the 250 beams in a single MBFEX tube, 154 were used for testing and analysis. For high power testing, the MBFEX tube was operated continuously at >3 kW to test the full functionality of the tube; the prototype CT typically operate at a lower power of ~ 1100 watts. Imaging detectors sample X-ray signals regularly for multiple 15-second datasets (adequate time for CT imaging of a meter-long bag) during a 4 hour span in response to a request from a leading system integrator to evaluate the MBFEX tube performance for baggage screening. The mean and standard deviation of normalized detector measurements (the individual detector measurements from each beam divided by the mean of all detector measurements of the same beam) within each dataset are computed separately for each of the 154 beams and the maximum, mean and minimum values of all the beams are plotted over time (Fig. 3).

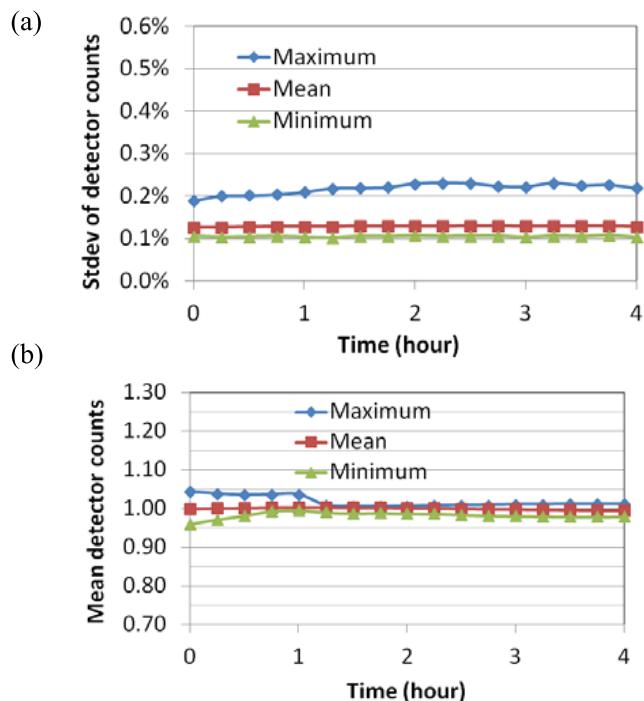


FIGURE 3. Stability of the MBFEX tube over time at 3.2 kW output. (a): Short-term (standard deviation of detector counts in a dataset). (b) Long-term (mean of detector counts in a dataset).

The measured long-term stability demonstrates the MBFEX tube delivers consistent X-ray dose from all 154 views over the full testing period. The variation in dose is below the MBFEX tube design limit (5%) and the measured maximum short-term instability remains well below the design limit (1%) throughout the testing period. This performance suggests the reliability of the MBFEX tube X-ray output measured by the imaging detector at high power is excellent and stable over time. The stability measured on the MBFEX tube is comparable to that of conventional X-ray tubes, but was achieved at a combination of high continuous operating power and small focal spot size that is prohibitive to conventional tubes.

III. SYSTEM AND GEOMETRY

Conventional CT systems are constrained to a circular imaging geometry due to the need to physically rotate an X-ray source to acquire tomographic data. CNT multibeam tubes provide an array of fixed X-ray focal spots that can be arranged in any geometry. Using CNT multibeam tubes, a CT system can be designed with an imaging geometry tailored to a specific imaging problem. We have used the MBFEX tubes to design a rectangular CT imaging geometry for an airport checkpoint baggage screening system (Fig. 4). At the airport checkpoint, space is limited and a full-sized rotating gantry CT does not fit into existing screening lanes.

To reduce the size of the imaging system, we arranged the X-ray focal spots and detectors to match the rectangular

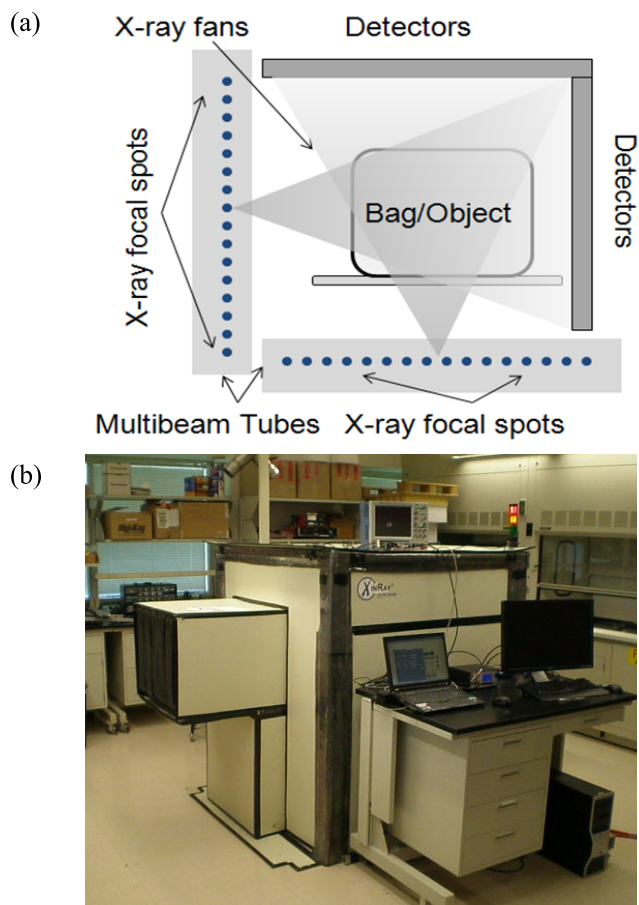


FIGURE 4. Laboratory prototype fixed gantry rectangular computed tomography system for airport checkpoint baggage screening. (a) Schematic representation of imaging geometry with linear arrays of focal spots arranged opposite linear detector arrays to form a rectangular scan around a tunnel with conveyor belt to move baggage through the CT scan. (b) The prototype in XinRay's laboratory.

lar shape of the imaging tunnel used by airport baggage screening systems. The system is an example of using CNT multibeam tubes to create a CT imaging geometry around a specific application rather than trying to fit an imaging application into a circular geometry.

The rectangular CT prototype is an improvement on the rectangular imaging setup presented at SPIE Medical Imaging 2013 [10]. The previous imaging setup used similar CNT multibeam tubes with a rectangular CT imaging geometry and was also designed for airport checkpoint baggage screening. The new CT prototype has several key design changes that improve the imaging geometry for both size and image quality. The changes made include: moving the X-ray parallel to the conveyor belt from above the tunnel to below the tunnel, increasing the length of the linear array of focal spots, changing the configuration of the detector elements, and changing the distribution of the focal spots used in a CT scan.

In the previous imaging setup, the CNT multibeam tube parallel to the conveyor belt was placed above the imaged

tunnel; by moving the tube below the belt, the height of the imaging system was significantly reduced. The total length of the linear array of X-ray focal spots was increased in the new prototype. Increasing the length of the array increased the angular coverage of the CT scan, improving the image quality in the reconstructed images. In addition to changing the length, we more evenly spread the distribution of X-ray focal spots to improve angular coverage. In the previous system, the focal spots were more consolidated; by spreading the focal spots the distribution of X-ray dose was more evenly spread over the different projection angles. The configuration of the detectors roughly followed an L shape in the previous imaging setup (Fig. 4). In the new prototype, the detectors have more of a U shape, also increasing angular coverage.

A parallelized sinogram of the imaging setup in [10] and the new laboratory prototype (Fig. 5) show the impact of the changes in the imaging geometry on the angular coverage. The parallelized sinograms are the result of a fan beam rebinning to a parallel beam sinogram based on the rectangular geometry. The parallel sinograms have large blank regions that are due to the sparse-view sample of the CT system and the relatively dense angular sampling in the parallel sinogram space. The blank regions are also due to the missing angular coverage resulting from a rectangular geometry [10]. The changes in the detector configurations and distribution of X-ray focal spots in the new prototype spread the coverage more evenly over the parallel sinogram (Fig. 5.b) and reduce the size of any single blank region. The reconstruction method can more easily account for the smaller blank regions than the several large regions.

The laboratory prototype has sparse angular sampling (Fig. 5); a number of angles are undersampled or not sampled at all. The angular sparsity is due to both the rectangular geometry and the total number of X-ray focal spots used in the CT scan. Two MBFEX tubes, each with 250 individually controllable focal spots (Section II), are used in the prototype. Not all of the focal spots from each tube are used when taking a CT scan. An airport baggage screening CT requires a high baggage throughput rate to reduce the passenger screening time. The number of X-ray focal spots is optimized to increase the speed of the CT scan.

IV. RECONSTRUCTION METHOD

We used a compressed sensing-based reconstruction method applying a total variation minimization algorithm to account for the sparse angular sampling. The reconstruction method is based on a modification of the adaptive-steepest descent projection onto convex sets (ASD-POCS) method [22]. For reconstruction, a volume is defined as a three-dimensional vector $F = F(x, y, z)$. We reconstruct the three-dimensional data by slice rather than by volume because we are using ultra-high speed fan beam data. Thus, the image vector is defined as $\vec{f} = f(x, y) = f_i \forall i = 0, 1, \dots, P$ for $P = N \cdot M$ where N is the number of image voxels in direction x and M is the number of image voxels in direction y for each slice

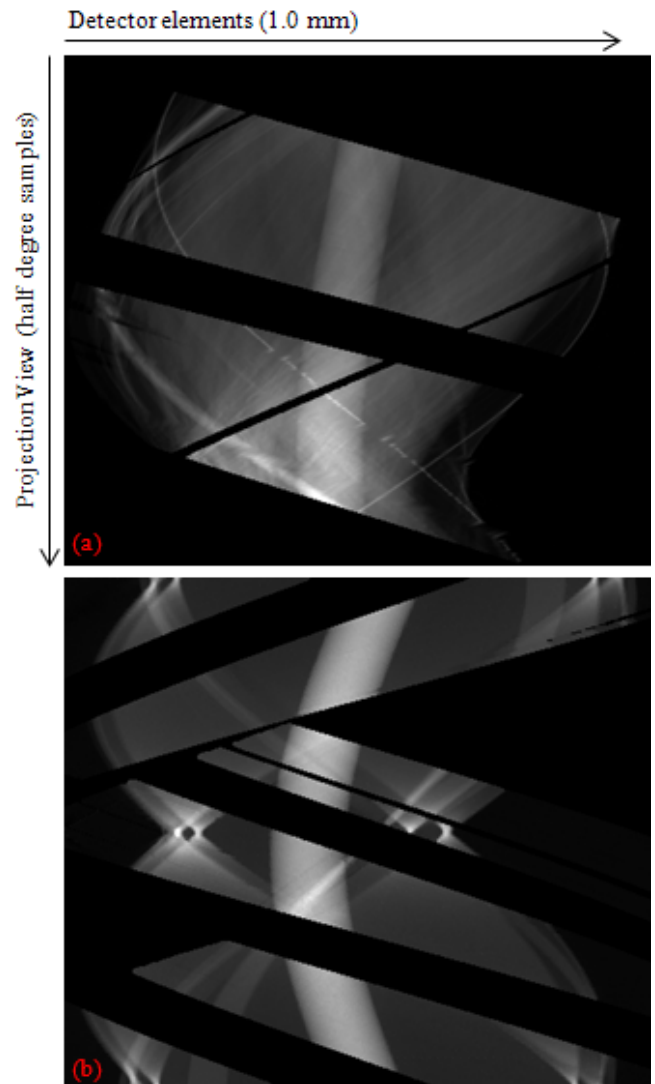


FIGURE 5. Parallelized sinograms applied to log corrected data for rectangular CT geometries. Two sinograms are scans of different objects are shown here for demonstrative purposes. (a) Parallelized sinogram of the previous imaging setup [10]. (b) Parallelized sinogram for new laboratory prototype. In both (a) and (b) the black background indicates missing data due to the sparse projection view sampling and rectangular imaging geometry.

$z = 0, 1, \dots, Z$ for a total of Z slices. The X-ray projections g_{data} are sampled as fan-beam projections for $j = 0, 1, \dots, \theta$ views for each slice z . The fan-beam projections are rebinned to a parallel-beam sinogram for each slice (Fig. 5). The ASD-POCS describes the optimal estimate of the image vector \vec{f} as

$$\vec{f}^* = \operatorname{argmin} \|\vec{f}\|_{TV} \quad \text{such that } |g(\vec{f}) - g_{data}| < \varepsilon \text{ and } \vec{f} \geq 0. \quad (1)$$

In (1), the value $\|\vec{f}\|_{TV}$ is the total variation in the image vector. The total variation is minimized subject to a constraint on the data error. In the error term, the function $g(\vec{f})$ relates the image vector to the projection data and for the ASD-POCS

algorithm this term is defined as

$$g(\vec{f}) = A\vec{f} \quad (2)$$

where A is a matrix with rank $\theta \cdot P$. The matrix A defines the relationship between each image location f_i and each X-ray projection g_j and is commonly referred to as the system matrix. When (2) is used to calculate the data constraint in (1) the projection data term g_{data} is log corrected where I_0 is the X-ray signal with only air in the tunnel and I_{data} is the measured signal.

$$g_{data} = \ln \frac{I_0}{I_{data}} \quad (3)$$

where I_0 is the X-ray signal with only air in the tunnel and I_{data} is the measured signal. Applying (3) removes all information about the variation of X-ray dose from the iterative reconstruction algorithm and transforms the measurements to a linear scale. The rectangular geometry has a large variation of dose over different angles based on the different X-ray path lengths and different angles at which the X-rays intersect the detector array. To include the variation in X-ray dose into the iterative reconstruction model, we changed the function $g(\vec{f})$ to include a measure of the X-ray signal through air I_0 . The new function relating the X-ray projections to the image vector is

$$g(\vec{f}) = I_0 \exp(-A\vec{f}). \quad (4)$$

When (4) is used for the data constraint in (1) the projection data term is the sample X-ray intensity $g_{data} = I_{data}$. Therefore, both the measure of X-ray signal through air and the X-ray intensity through an object are now included in the reconstruction model.

To solve (1) we apply an adaption of the ASD-POCS method where the POCS is modified based on the new data term (4). The original POCS term was solved using an ART which fits the linear system (2). We use an ordered subset convex (OSC) algorithm instead, similar to an approach taken by Jia [33] but our algorithm retains the ASD step; we call the algorithm ASD-OSC. The pseudo code for our reconstruction algorithm is:

$$\vec{f}^n \leftarrow \vec{f}^* \quad (5.1)$$

$$\vec{f}^{n+1} = \vec{f}^n + \beta \cdot \vec{f}^n \cdot \frac{\partial}{\partial f} |g(\vec{f}^n) - I_{data}| \quad (5.2)$$

$$\vec{f}^* = \operatorname{argmin} \|\nabla \vec{f}^{n+1}\|_1 \quad (5.3)$$

$$\vec{f}^* \geq 0 \quad (5.4)$$

$$\text{repeat until converged} \quad (5.5)$$

To solve the data term, we use the OSC [34] algorithm

$$f_i^{n+1} = f_i^n + \beta \cdot f_i^n \times \frac{\sum_{j \in S} a_{ij} \left[I_{0j} \exp\left(-\sum_i a_{ij} f_i^n\right) - I_{data,j}\right]}{\sum_{j \in S} a_{ij} \left[\left(-\sum_i a_{ij} f_i^n\right) \cdot \left(I_{0j} \exp\left(-\sum_i a_{ij} f_i^n\right)\right)\right]} \quad (6)$$

similar to the algorithm used by Quan and Lalush [18] and applied to a non-circular fixed gantry CT. The use of an ordered subset algorithm in place of ART accelerates the convergence of the algorithm. When the OSC algorithm is implemented independently for a non-circular sparse-view CT, the limited-angle artifacts can degrade the image quality. By combining the total variation minimization with the OSC, the artifact suppression of the total variation method suppresses the sparse-view and missing angle artifacts. The ASD approach allows the strength of the total variation minimization to decay based on a constant and the OSC includes a β constant that can change with iterations to reduce the impact of the data term. Increasing the ASD decay rate reduces the impact of the total variation minimization on the final reconstruction and increases the sharpness but also the noise and artifacts in the reconstructions. Decreasing the β reduces the impact of the data term and creates a smoother image with fewer artifacts but it also suppresses the resolution in the image.

We found that a $\beta = 1$ and an aggressive ASD decay resulted in the best image quality with the fastest reconstruction time. However, this configuration resulted in a relatively large amount of noise and artifacts remaining in the image. To further suppress the artifacts in the final reconstruction we added a bilateral filter as a post processing set [35]. The bilateral filter is defined as

$$f_i = K_i \sum_{j \in \Omega} f_j \cdot \exp\left(-\frac{(j-i)^2}{2\sigma_d^2}\right) \cdot \exp\left(-\frac{(f_j - f_i)^2}{2\sigma_r^2}\right) \quad (7)$$

for a neighbor $j \in \Omega$ with respect to voxel i . The constant K is a normalization factor to normalize the gain of the filter to 1.0. The bilateral filter applies two Gaussian smoothing functions, one over the spatial neighborhood Ω and the other based on the difference of the voxel intensities at each location in the neighborhood. By applying a Gaussian smoothing weight to the difference in voxel intensities, only voxels with similar intensity values will smooth over the neighborhood; this intensity weighting preserves the edges in the image. We apply the bilateral filter using a three-dimensional neighborhood to allow the slice to slice consistency within objects to further suppress the noise and image artifacts. We use a large spatial neighborhood and standard deviation σ_d and a small intensity standard deviation σ_r to preserve soft edges within the image.

V. GPU IMPLEMENTATION

The goal for our reconstruction algorithm is to implement the iterative reconstruction algorithm (5) in real-time using a GPU. We define real-time as reconstructing an object two thirds of a meter long in less than five seconds. The initial implementation of the ASD-POCS algorithm for the imaging setup (Fig. 4.a) took approximately 17 hours to reconstruct a full volume. Over time a number of improvements, including implementing the algorithm on different GPUs, optimizing the GPU implementation, and moving to an ordered subset algorithm, has reduced the total reconstruction time (Table 1).

TABLE 1. Algorithm speed.

Algorithm Implementation	Reconstruction Time (sec)
ASD-POCs on CPU	62,400
ASD-POCs on Quadro FX 550 GPU	3,120
ASD-POCs CUDA Optimization	2,163
ASD-POCs on GeForce GT 640 GPU	516
ASD-POCS Additional Optimization	160
ASD-OSC on GeForce GT 640 GPU	51
ASD-OSC on GeForce GT 780 TI GPU	6.8*

List of total time it takes to reconstruct a 608x416x416 voxel volume based on different reconstruction algorithms and hardware implementations. All times are based on the same convergence criteria rather than total number of iterations because the use of ordered subsets changes the rate of convergence. * Estimated time based on number of GPU cores (not currently implemented)

We have implemented the entire reconstruction algorithm, including the bilateral filter, on a GPU; this allows us to limit the large memory transfers to loading the projection data onto the GPU and removing the data off the GPU. We load a subset of projection slices simultaneously and reconstruct the slices at the same time. Reconstructing a set of slices simultaneously allows us to reduce the number of geometry calculations required for the projection and backprojection steps in (6) by applying the same calculation to all slices simultaneously. The ASD step requires more decision steps based on the l_1 -norm of each reconstructed slice. To increase the speed, the simultaneous slices are broken into memory streams on the GPU [36] and the decision calculations are rapidly made on the CPU for each slice and then passed back to the GPU. The use of memory streams allows for an overlap between the memory transfers to the CPU and continued GPU calculations to limit the loss in computation time due to the ASD decisions. The current reconstruction implementation takes approximately 51 seconds to reconstruct a volume 0.667 meters long. We are currently using a GeForce GT 640 GPU that has 384 cores. By upgrading the GPU to a GeForce GT 780 TI, we would increase the number of cores to 2880; this is 7.5 times the number of cores on the current GPU. By increasing the number of slices loaded simultaneously, we can take full advantage of the increased number of GPU cores and decrease the reconstruction speed to approximately 6.8 seconds.

VI. EXPERIMENTAL RESULTS

In this section, we present experimental data collected using the laboratory prototype CT system. All of the data was collected using an 11.2 cm/sec conveyor belt speed. The data was acquired as fan-beam spiral CT. At 11.2 cm/sec, the fixed gantry CT system has an equivalent rotation speed of 70 Hz; 70 CT slices are taken every second resulting in 1.6 mm thick fan-beam slices. The CNT multibeam tubes were operated at 7 milliamperes anode current with a 160 kVp anode voltage. Airport baggage screening systems typically have to run at much lower X-ray current to preserve the lifetime of the tubes because these systems are on continuously for

12 to 16 hours a day. They also typically operate with higher energy X-rays because the range of object densities is broader than in medical imaging; passengers travel with everything from very low density cotton clothing to very high density electronics and tools.

The prototype CT system uses linear arrays of integrating detectors with 1.6 mm pitch. The X-ray projections are rebinned to a 1.0 mm pitch over a 180° span with a 0.5° sampled parallel beam sinogram (Fig. 4). The reconstruction volume is defined by 1.0 mm by 1.0 mm by 1.6 mm voxels for a 608.0 mm by 416.0 mm by 665.6 mm volume. The rectangular volume is defined to fit the typical 600.0 mm by 400.0 mm imaging tunnel used by current airport checkpoint X-ray baggage screening systems [37].

To test the new laboratory prototype, we followed the American National Standard for Evaluating the Image Quality of X-Ray Computed Tomography (CT) Security-Screening Systems IEEE [38]. This standard uses two imaging phantoms, referred to as Article A and Article B. The Article A phantom focuses on image artifacts, primarily beam hardening and X-ray scatter artifacts. The Article B phantom focuses on image resolution and noise, measuring the point spread function (PSF), the modulation transfer function (MTF), and the noise. We imaged both Article A and Article B using the laboratory prototype and compared the results with a conventional CT scan of both phantoms.

The medical CT scan used for comparison was a Siemens SOMATON Definition CT set for an Adult thorax scan. The scan was done at 140keV X-ray energy, a 7 milliamperes X-ray dose, a 500 millisecond exposure time, and 1.2 mm X-ray focal spot size. The reconstructed volume was 512 by 512 by 802 with 1.27 mm by 1.27 mm by 1.00 mm pixels in x, y, and z respectively. The imaging settings were not optimized for the Article A and B phantoms and the phantom was slightly larger than the field of view, resulting in significant blur on one side of the reconstruction. The images were reconstructed using Siemens Syngo CT software version 2010 A. The reconstruction software was not optimized for low X-ray dose; CT scans taken with a high X-ray dose (not shown in this paper) provided much better image quality. Reconstruction images from the Siemens system were used for comparative purposes and do not represent the actual image quality of the system when used properly (for diagnostic medical imaging, not security screening).

A reconstructed slice from Article A (Fig. 6) shows an acetabular cylinder 7.5 cm in diameter with four tungsten pins 0.15 cm in diameter centered along a 3.18 cm radial distance from the center of the acetabular cylinder. The tungsten pins cause significant streaking artifacts in the conventional CT reconstruction (Fig. 6.a). If filtered back projection (FBP) is applied to the laboratory prototype, the streaking artifacts along with the limited-angle artifacts cause significant distortion in the reconstructed image. The different proposed iterative reconstruction algorithms ASD-POCS, OSC, and ASD-OSC all suppress the streaking artifacts and produce

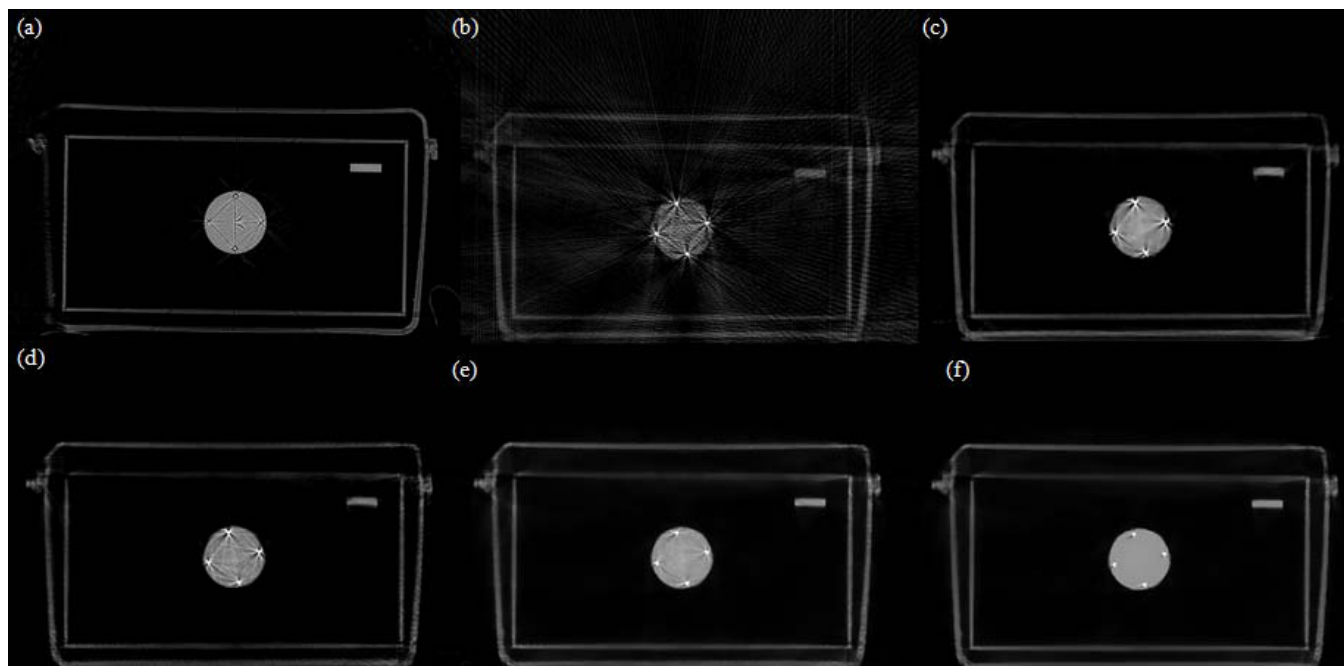


FIGURE 6. Reconstructed slice of Article A phantom, which includes an acetal cylinder with four tungsten pins. All images are shown on a -750 to 1500 Hounsfield Units scale. (a) Medical CT reconstruction of phantom reconstructed using filtered back projection (FBP). (b)-(f) are all reconstructions using different algorithms based on data from the laboratory prototype. (b) FBP reconstruction. (c) ASD-POCS reconstruction. (d) OSC reconstruction. (e) ASD-OSC reconstruction. (f) ASD-OSC with bilateral filtering reconstruction.

TABLE 2. Reconstruction artifact metrics (ratio with control).

Algorithm and Geometry	20 cm Acetal	35 cm Acetal	Mean AI Ring	Std AI Ring
Medical CT	0.93	0.79	1.02	1.94
ASD-POCS Old Geometry	0.78	0.59	1.05	3.75
ASD-POCS New Geometry	0.85	0.63	1.09	1.83
ASD-OSC New Geometry	0.93	0.87	1.09	1.11
ASD-OSC + Bilateral Filter New Geometry	0.93	0.87	1.09	1.04

Comparing different image artifact metrics for different iterative reconstruction algorithms and imaging geometries. Old geometry is the previous imaging setup [10] and new geometry is the laboratory prototype (Section III). The 20 cm and 35 cm give the ratio of the mean of an ROI inside an acetal block 20 cm and 35 cm thick compared to the mean of the same ROI of an acetal block 3.8 cm thick. The mean and standard deviation are the ratio of an ROI inside an acetal cylinder surrounded by an aluminum ring compared with the same ROI with no ring.

higher image quality. By adding the bilateral filter (Fig. 6.f) the artifacts are almost entirely suppressed and the detail in the image preserved.

The results for other Article A image artifacts are shown in Table 2. In Table 2, all of the values are the ratio of the measurement compared to a control; thus, the optimal value for each measurement is 1.0. The mean of a 2 cm by 1.4 cm ROI located in the center of an acetal block that has fan shape with a thickness 1.4 cm and a length distributed between 3.8 cm and 39.4 cm is compared by taking the ratio of the mean for a given length with the minimal length to measure

TABLE 3. Image quality metrics.

Algorithm and Geometry	PSF	PSF (Z)	MTF	% STD
Medical CT	1.5 mm	3.6 mm	14.6 cm^{-1}	10.33
ASD-POCS Old Geometry	3.5 mm	1.6 mm	4.3 cm^{-1}	14.5
ASD-POCS New Geometry	2.5 mm	1.7 mm	6.5 cm^{-1}	7.6
ASD-OSC New Geometry	1.89 mm	1.4 mm	7.5 cm^{-1}	4.2
ASD-OSC + Bilateral Filter New Geometry	1.35 mm	1.35 mm	10.5 cm^{-1}	2.2

Comparing different image quality metrics for different iterative reconstruction algorithms and imaging geometries. Old geometry is the imaging setup [5] and new geometry is the laboratory prototype (Section III). The values for full width at half maximum (FWHM) for the point spread function (PSF) measured by the Article B phantom are labeled PSF. The values for the FWHM of the PSF measured between slices are labeled (PSF(Z)). The frequency at 10% of the modular transfer function (MTF) is measured by the phantom, the medical CT MTF is better due to a post-processing sharpening filter applied as a part of the Syngo software. The % STD is the standard deviation compared to the mean measured using the acetal cylinder.

the effects of beam hardening and scatter due to a long path length through a homogenous material. The mean and standard deviation for a 4 cm by 4 cm ROI located in the center of an acetal cylinder inside of a ring of 1.14 cm thick aluminum are compared with the mean and a standard deviation of similar ROI inside an acetal cylinder with no ring. For the measurement from inside of the aluminum ring the beam hardening artifact shifts the mean slightly and this result is slightly worse in the new geometry due to redistribution

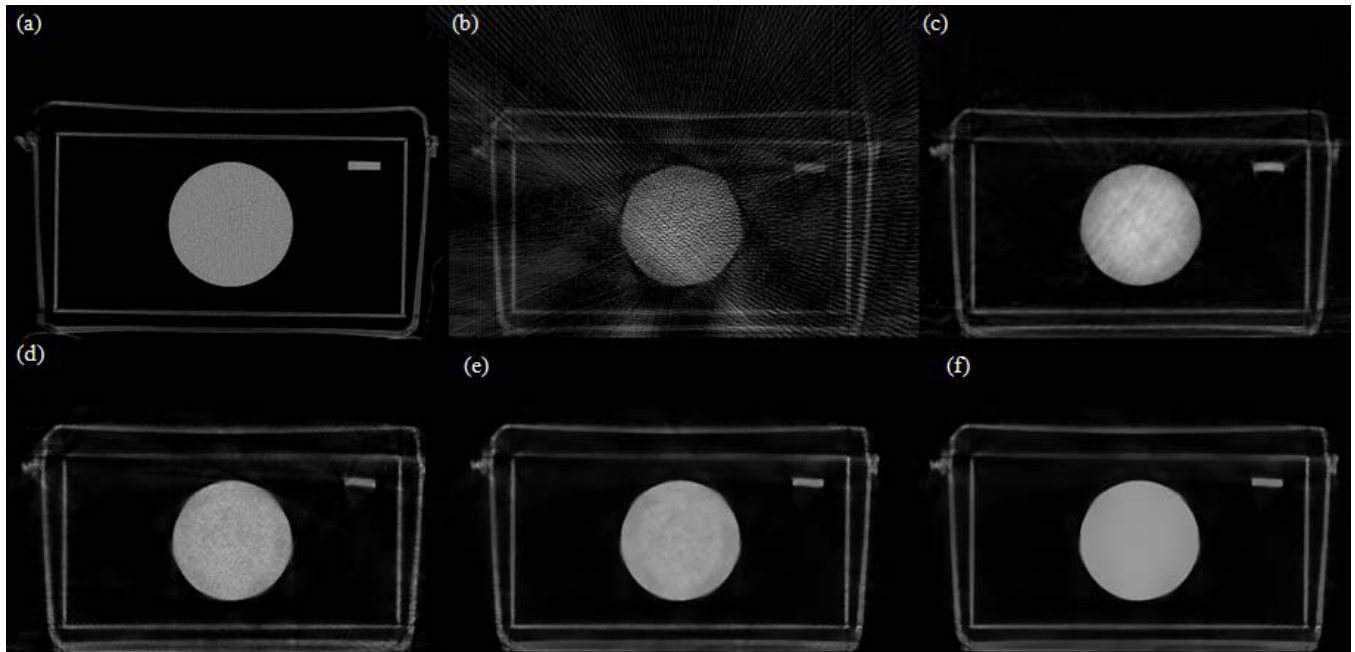


FIGURE 7. Reconstructed slice of the Article B phantom large acetal cylinder used to measure PSF, MTF and noise. All images shown are on a -750 to 1500 Hounsfield Units scale. (a) Medical CT reconstruction of the phantom reconstructed using filtered back projection (FBP). (b)-(f) are all reconstructed using different algorithms based on data from the laboratory prototype. (b) FBP reconstruction. (c) ASD-POCS reconstruction. (d) OSC reconstruction. (e) ASD-OSC reconstruction. (f) ASD-OSC with bilateral filtering reconstruction.

of detectors. In the other measurements, the laboratory prototype scan with the ASD-OCS reconstruction algorithm resulted in a measurement close to or better than the conventional CT scan.

A reconstructed slice from Article B (Fig. 7) shows an acetal copolymer cylinder 14.8 cm in diameter. The large cylinder absorbs a significant amount of X-ray dose resulting in a large amount of noise within the reconstructed cylinder. FBP is applied to the laboratory prototype, the low dose increases the effect of the limited-angle artifacts and the noise within the cylinder is large compared to the mean reconstructed value of the cylinder. The different proposed iterative reconstruction algorithms ASD-POCS, OSC, and ASD-OSC all suppress the limited-angle artifacts and produce lower noise resulting in higher image quality. By adding the bilateral filter (Fig. 7.f) the artifacts and noise are almost entirely suppressed. The measure of noise is shown in Table 3 as a percentage of the mean of the cylinder. The conventional CT (Fig. 7.a) has a high degree of noise due to the low dose level.

The results for other Article B image quality measurements are shown in Table 3. In Table 3, the values are calculated using the large acetal cylinder (Fig. 7) but are averaged over multiple slices to suppress the noise in the calculations. The point spread function (PSF) is measured by summing along the edge derivative of the cylinder; thus the PSF accounts for loss of resolution at different angles. The previous imaging setup had very poor calculated PSF due to the large regions of missing angular samples

(Fig. 5). The use of OSC reduced the blur along the edge, further improving the PSF. The bilateral filter suppressed noise along the edge enhancing the sharpness of the edge. The PSF between reconstructed slices is calculated using the edge of a slanted block of acetal. The high equivalent CT rotation speed of the fixed gantry CT provides a high sampling rate between slices and high resolution in all three-dimensions. The MTF was calculated by taking the Fourier transform of the PSF in the x-y plane. The MTF captures the loss of resolution due to incomplete angular sampling. The MTF for the medical scan is better than the MTF for the ASD-OSC even though the PSF for the medical is slightly lower. The PSF is measured at 50% whereas the MTF is measured at 10% . The small distortions in the cylinder cause a small loss in the high frequency accuracy seen in the measurement of the MTF. Fig. 7 shows that all of the cylinders sampled by the prototype are not perfectly circular and have small distortions where data is missing.

To demonstrate the laboratory prototype CT with a more realistic object, we scanned a suitcase filled with a number of objects of interest and clothing. In Fig. 8, a three-dimensional rendering of the reconstructed suitcase is shown. Additionally the three-dimensional rendering of a number of objects of interest are shown separately, isolated from the suitcase data. The objects of interest include bottles filled with liquid, a knife, a cell phone, a bottle of wine, a laptop, and a personal grooming kit. The objects are isolated to show that the detail in the different objects is accurately reconstructed.

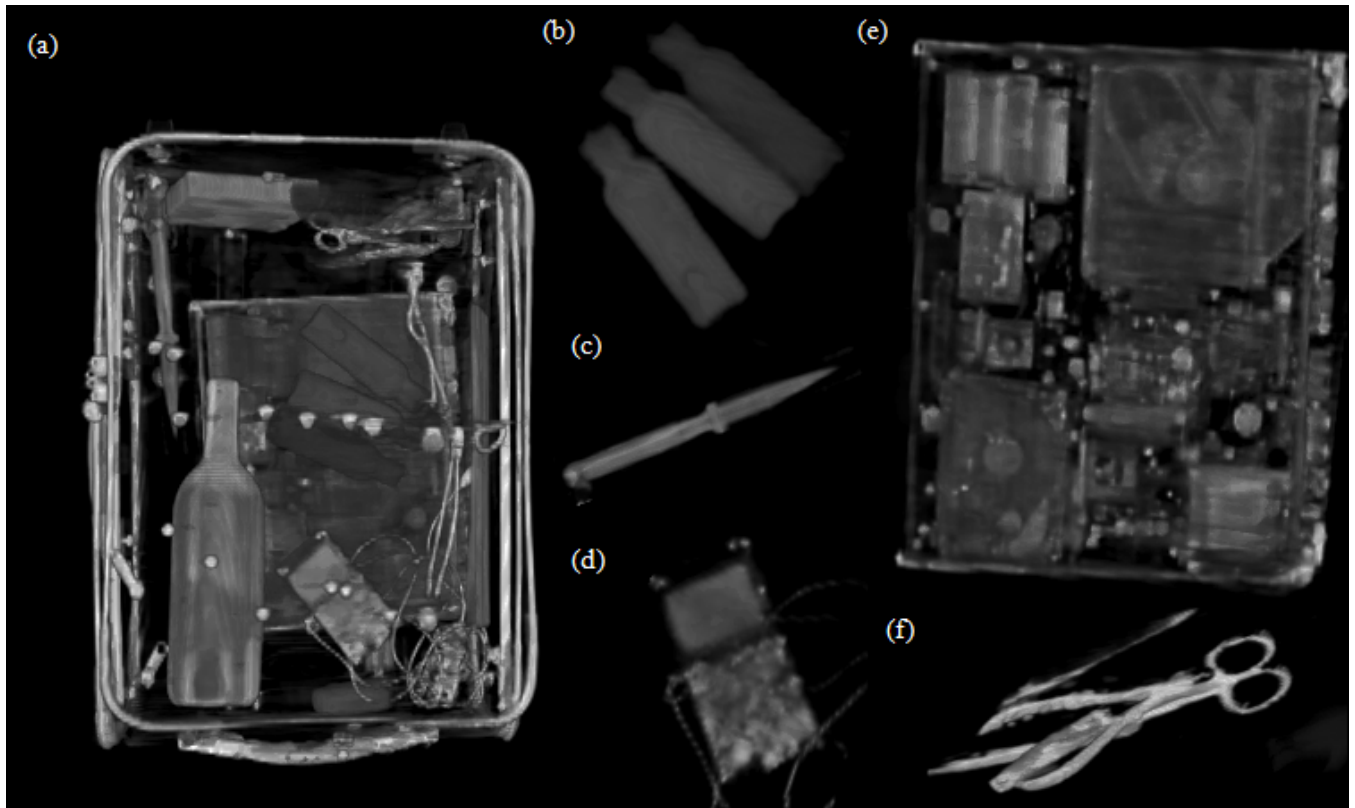


FIGURE 8. Three dimensional rendering of a reconstruction of a suitcase scanned using the prototype CT. The image includes (a) full rendering of suitcase, (b) multiple bottles filled liquids, (c) a knife, (d) a cell phone, (e) a laptop computer, and (f) a personal grooming kit with multiple objects.

The 3D rendering of the different objects demonstrates the high resolution and accuracy of the prototype system and reconstruction method.

VII. CONCLUSION

A laboratory prototype CT that utilizes an advanced CNT multibeam tube to create a unique CT imaging scanner designed specifically for airport checkpoint baggage screening has been presented. The prototype demonstrated the use of new X-ray sources and iterative reconstruction algorithms to customize a CT to a specific imaging challenge. The concepts presented, including: CNT multibeam tubes, non-circular CT geometries, and accelerated compressed sensing iterative reconstruction algorithms, can also be used to design CT solutions for many other imaging challenges. The CNT multibeam tubes can be designed to deliver a wide range of X-ray dose levels and are built with any number of unique focal spot distributions to accommodate even more exotic tomographic geometries. Iterative reconstruction algorithms can be used with the unique geometries and provide reconstructed image quality comparable to conventional CT and implemented in real-time on GPUs. The unique combination of CNT multibeam tubes and accelerated iterative algorithms opens the door to a new generation of CT systems designed and optimized specifically for a given imaging application.

ACKNOWLEDGMENT

We would like to thank Dr. Yueh Lee of the Department of Radiology, University of North Carolina, for his assistance in acquiring the medical CT images.

REFERENCES

- [1] R. H. Fowler and L. Nordheim, "Electron emission in intense electric fields," *Proc. Roy. Soc. London Ser. A, Contain. Papers Math. Phys. Character.*, vol. 119, no. 781, pp. 173–181, 1928.
- [2] Y. Cheng and O. Zhou, "Electron field emission from carbon nanotubes," *Comptes Rendus Phys.*, vol. 4, no. 9, pp. 1021–1033, 2003.
- [3] X. Calderón-Colón, H. Geng, B. Gao, L. An, G. Cao, and O. Zhou, "A carbon nanotube field emission cathode with high current density and long-term stability," *Nanotechnology*, vol. 20, no. 32, p. 325707, 2009.
- [4] X. Qian et al., "High resolution stationary digital breast tomosynthesis using distributed carbon nanotube x-ray source array," *Med. Phys.*, vol. 39, no. 4, pp. 2090–2099, 2012.
- [5] D. Shiffler, O. Zhou, C. Bower, M. LaCour, and K. Golby, "A high-current, large-area, carbon nanotube cathode," *IEEE Trans. Plasma Sci.*, vol. 32, no. 5, pp. 2152–2154, Oct. 2004.
- [6] M. Hadsell et al., "A first generation compact microbeam radiation therapy system based on carbon nanotube X-ray technology," *Appl. Phys. Lett.*, vol. 103, no. 18, p. 183505, 2013.
- [7] A. W. Tucker, J. Lu, and O. Zhou, "Dependency of image quality on system configuration parameters in a stationary digital breast tomosynthesis system," *Med. Phys.*, vol. 40, no. 3, p. 031917, 2013.
- [8] F. Sprenger et al., "Distributed source X-ray tube technology for tomosynthesis imaging," *Proc. SPIE*, vol. 7622, p. 76225M, Mar. 2010.
- [9] F. Sprenger et al., "Stationary digital breast tomosynthesis with distributed field emission X-ray tube," *Proc. SPIE*, vol. 7961, p. 79615I, Mar. 2011.
- [10] B. Gonzales et al., "Rectangular computed tomography using a stationary array of CNT emitters: Initial experimental results," *Proc. SPIE*, vol. 8668, p. 86685K, Mar. 2013.

- [11] J. Zhang et al., "Stationary scanning X-ray source based on carbon nanotube field emitters," *Appl. Phys. Lett.*, vol. 86, no. 18, p. 184104, 2005.
- [12] X. Qian et al., "Design and characterization of a spatially distributed multi-beam field emission X-ray source for stationary digital breast tomosynthesis," *Med. Phys.*, vol. 36, no. 10, pp. 4389–4399, 2009.
- [13] G. Cao et al., "A dynamic micro-CT scanner based on a carbon nanotube field emission X-ray source," *Phys. Med. Biol.*, vol. 54, no. 8, pp. 2323–2340, 2009.
- [14] L. Yueh et al., "Prospective respiratory gated carbon nanotube micro computed tomography," *Acad. Radiol.*, vol. 18, no. 5, pp. 588–593, 2011.
- [15] L. T. Niklason et al., "Digital tomosynthesis in breast imaging," *Radiology*, vol. 205, no. 2, pp. 399–406, 1997.
- [16] E. Quan and D. S. Lalush, "Three-dimensional imaging properties of rotation-free square and hexagonal micro-CT systems," *IEEE Trans. Med. Imag.*, vol. 29, no. 3, pp. 916–923, Mar. 2010.
- [17] E. Quan and D. S. Lalush, "A faster ordered-subset convex algorithm for iterative reconstruction in a rotation-free micro-CT system," *Phys. Med. Biol.*, vol. 54, no. 4, pp. 1061–1072, 2009.
- [18] H. Erdogan and J. A. Fessler, "Ordered subsets algorithms for transmission tomography," *Phys. Med. Biol.*, vol. 44, no. 11, pp. 2835–2851, 1999.
- [19] D. S. Lalush and B. M. W. Tsui, "Fast transmission CT reconstruction for SPECT using a block-iterative algorithm," *IEEE Trans. Nucl. Sci.*, vol. 47, no. 3, pp. 1123–1129, Jun. 2000.
- [20] R. R. Galigekere, K. Wiesent, and D. W. Holdsworth, "Techniques to alleviate the effects of view aliasing artifacts in computed tomography," *Med. Phys.*, vol. 26, no. 6, pp. 896–904, 1999.
- [21] A. H. Andersen, "Algebraic reconstruction in CT from limited views," *IEEE Trans. Med. Imag.*, vol. 8, no. 1, pp. 50–55, Mar. 1989.
- [22] X. Pan, E. Y. Sidky, and M. Vannier, "Why do commercial CT scanners still employ traditional, filtered back-projection for image reconstruction?" *Inverse Problems*, vol. 25, no. 12, p. 123009, 2009.
- [23] E. Y. Sidky, C. Kao, and X. Pan, "Accurate image reconstruction from few-views and limited-angle data in divergent-beam CT," *J. X-Ray Sci. Technol.*, vol. 14, no. 2, pp. 119–139, 2006.
- [24] E. Y. Sidky, R. Chartrand, and X. Pan, "Image reconstruction from few views by non-convex optimization," in *Proc. IEEE Nucl. Sci. Symp. Conf. Rec. (NSS)*, vol. 5, Nov. 2007, pp. 3526–3530.
- [25] Y. Zhang, B. Dong, and Z. Lu, " ℓ_0 minimization for wavelet frame based image restoration," *Math. Comput.*, vol. 82, no. 282, pp. 995–1015, 2013.
- [26] E. J. Candès, J. Romberg, and T. Tao, "Robust uncertainty principles: Exact signal reconstruction from highly incomplete frequency information," *IEEE Trans. Inf. Theory*, vol. 52, no. 2, pp. 489–509, Feb. 2006.
- [27] B. Adcock, A. C. Hansen, and B. Roman. (2014). "The quest for optimal sampling: Computationally efficient, structure-exploiting measurements for compressed sensing." [Online]. Available: <http://arxiv.org/abs/1403.6540>
- [28] W. Han, H. Yu, and G. Wang, "A general total variation minimization theorem for compressed sensing based interior tomography," *Int. J. Biomed. Imag.*, vol. 2009, Jan. 2009, Art. ID 125871.
- [29] H. Yu, and G. Wang, "A soft-threshold filtering approach for reconstruction from a limited number of projections," *Phys. Med. Biol.*, vol. 55, no. 13, p. 3905, 2010.
- [30] K. Mueller and R. Yagel, "Rapid 3-D cone-beam reconstruction with the simultaneous algebraic reconstruction technique (SART) using 2-D texture mapping hardware," *IEEE Trans. Med. Imag.*, vol. 19, no. 12, pp. 1227–1237, Dec. 2000.
- [31] X. Jia, B. Dong, Y. Lou, and S. B. Jiang, "GPU-based iterative cone beam CT reconstruction using tight frame regularization," *Phys. Med. Biol.*, vol. 56, no. 13, pp. 3787–3807, 2010.
- [32] G. Prax and L. Xing, "GPU computing in medical physics: A review," *Med. Phys.*, vol. 38, no. 5, pp. 2685–2697, 2011.
- [33] X. Jia, Y. Lou, R. Li, W. Y. Song, and S. B. Jiang, "GPU-based fast cone beam CT reconstruction from undersampled and noisy projection data via total variation," *Med. Phys.*, vol. 37, no. 4, pp. 1757–1760, 2010.
- [34] C. Kamphuis and F. J. Beekman, "Accelerated iterative transmission CT reconstruction using an ordered subsets convex algorithm," *IEEE Trans. Med. Imag.*, vol. 17, no. 6, pp. 1101–1105, Dec. 1998.
- [35] C. Tomasi and R. Manduchi, "Bilateral filtering for gray and color images," in *Proc. 6th Int. Conf. Comput. Vis.*, Jan. 1998, pp. 839–846.
- [36] J. Nickolls, I. Buck, M. Garland, and K. Skadron, "Scalable parallel programming with CUDA," *Queue*, vol. 6, no. 2, pp. 40–53, 2008.
- [37] B. Elias, *Airport Passenger Screening: Background and Issues for Congress*. Collingdale, PA, USA: DIANE Publishing, 2009.
- [38] *American National Standard for Evaluating the Image Quality of X-Ray Computed Tomography (CT) Security-Screening Systems*, IEEE Standard N42.45-2011, 2011.

BRIAN GONZALES, photograph and biography not available at the time of publication.

DERREK SPRONK, photograph and biography not available at the time of publication.

YUAN CHENG, photograph and biography not available at the time of publication.

ANDREW W. TUCKER, photograph and biography not available at the time of publication.

MORITZ BECKMAN, photograph and biography not available at the time of publication.

OTTO ZHOU, photograph and biography not available at the time of publication.

JIANPING LU, photograph and biography not available at the time of publication.

• • •